Title	Zonal Proton Generation from Target Edges Using Ultra-Intense Laser Pulse
Author(s)	Yabuuchi, Toshinori; Habara, Hideaki; Tampo, Motonobu et al.
Citation	Plasma and Fusion Research. 2007, 2, p. 003
Version Type	VoR
URL	https://hdl.handle.net/11094/3115
rights	Copyright (c) 2007 The Japan Society of Plasma Science and Nuclear Fusion Research
Note	

Zonal Proton Generation from Target Edges Using Ultra-Intense Laser Pulse

Toshinori YABUUCHI[1,2], Hideaki HABARA[1,2], Motonobu TAMPO[2], Ryosuke KODAMA[1,2], Shinya AWANO[1,2], Kiminori KONDO[1,2], Kunioki MIMA[2] and Kazuo A. TANAKA[1,2]

[1)]*Graduate School of Engineering, Osaka University, Osaka 565-0871, Japan*
[2)]*Institute of Laser Engineering, Osaka University, Osaka 565-0871, Japan*

Multi MeV proton beam is generated via target normal sheath acceleration when the target is irradiated with an ultra-intense laser pulse. In addition, a unique structure, "zonal pattern", of energetic protons is observed in the perpendicular directions of the target edges using triangular targets. The sheath field production on the target edges may be responsible for this zonal pattern. Two dimensional particle-in-cell simulations show that the electrostatic field initially produced at around the cross point at the laser axis and the rear surface expands on the target surface in time. The field enhancement occurs at the target edges when the sheath field reaches there. The enhanced field can accelerate protons in a zonal pattern.

Multi MeV protons and heavy ions are generated in the ultra-intense laser (UIL) and matter interactions. These energetic particles may be utilized for core heating in the fast ignition scheme of laser fusion [1, 2], backlight source for imaging of fields or objects [3–5], isotope production [6,7], and proton therapy [8,9]. Light ions in the molecules covering the target surfaces are accelerated more easily than heavy ions which compose the target material. Accelerated particles are typically protons that exist as water molecules on the target surface. The sheath field is produced by a charge separation resulting from the laser accelerated hot electrons departing from the target. The sheath field pulls an energetic proton beam out of the target rear to the normal direction known as the target normal sheath acceleration (TNSA) [10]. Many experiments and simulations have been performed to investigate the generation mechanisms and the characteristics of proton beams generated by the UIL pulse using a solid target [11–13]. The proton emission has been also studied using shaped targets, such as hollow cones [14], wires [15], and foils with structured rear surface [16, 17]. The protons are accelerated by strong sheath fields even in such particular cases as well.

The emission pattern of the energetic protons generated by the TNSA is typically observed as a well-collimated beam, namely circular pattern, in experiments using simple foil targets. However, the detected pattern of protons has shown other structures, for example, a cross pattern [18]. These structures are normally observed for low energy protons. The mechanisms producing these structured patterns are not fully understood.

In this Letter, we present a unique emission structure of protons, "zonal pattern", observed around the circular pattern, and study mechanisms to produce the pattern. Using triangle-shaped foil targets in the UIL experiments, we obtain zonal patterns, which strongly depend on the target shape, spreading out perpendicular to the target edges. The production of the electrostatic sheath field is studied with a 2-dimensional (2D) particle-in-cell (PIC) simulation. The sheath field spreads out from the laser axis to the target edges on the target rear surface in time. The field strength is enhanced at the target edges when the sheath field reaches there. The field accelerates the protons at the target edges into wide angles resulting in production of the observed zonal patterns of protons.

The experiments are performed at the 30 TW laser facility at the Institute of Laser Engineering, Osaka University. The targets used in the experiments are all made of a 50-µm-thick aluminum foil. The target shape is an equilateral triangle whose edge length is 3 mm each. The target is supported by a glass stalk of a diameter 30 µm from the above. In the experiments, the target is set onto the stalk in two different directions; upward and downward as shown in Figs. 1 (a) and (b). The target is tilted 23° from a vertical plane for the *s*-polarized laser irradiation. Here, the laser polarization is in the horizontal direction. The laser pulse (1.053 µm wavelength) is focused on the center of the target via an off-axis parabolic mirror (F/3.8) resulting in a 15-µm-diameter spot with 40% of the laser energy.

In the experiments, the proton emission distribution is measured with a solid state track detector, CR-39 (Nagase Landauer: BARYOTRAK-P). Simultaneously, the hot
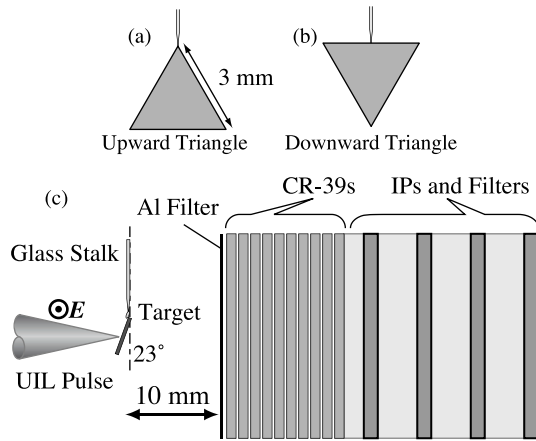
Fig. 1   Schematic of the experimental setup. The target is set
         onto a stalk in two different directions; (a) upward and
         (b) downward. (c) Side view of the target and the detector
         pack.

Fig. 2   (a) Electron emission distribution in the first layer of
         IP. The label "(up)" indicates the upward triangular tar-
         get case. Threshold energy for detection is calculated
         as 0.7 MeV. Proton emission distribution observed by
         (b) first and (c) second layers of CR-39 for the upward tri-
         angular target case. (d) Schematic of the observed image
         in the first layer of CR-39 for the upward triangular target
         case. The gray box (32 mm × 57 mm) corresponds to the
         particle detectable region. Proton emission distribution
         observed by the (e) first and (f) second layers of CR-39
         for the downward triangular target case. The energies of
         TNSA protons at 23° oblique incidence are 0.95 MeV for
         the first layer and 3.2 MeV for the second layer.

electron emission distribution is observed with an imaging
plate (IP) (Fuji Film: BAS-SR2025) [19]. Spatial distribu-
tions of energetic protons and electrons are detected with
a pack of multi-layered detectors at 10 mm from the tar-
get rear as shown in Fig. 1 (c). The detector pack is cov-
ered with a 12-μm-thick aluminum foil to shield the de-
tector surface from debris and strong scattered light. In
addition, polyethylene terephthalate layers are inserted to
remove the proton signal on IPs and to observe electron
distributions with discrete energies. The multilayered de-
tectors for protons (CR-39) and for electrons (IP) observe
the spatial distributions of the particles with the certain en-
ergies depending on the depth of the detector layer. The
detectable proton energies in each layer of CR-39 are es-
timated with a Monte-Carlo simulation code, TRIM [20].
Monte-Carlo simulation, EGSnrc [21], is used to calculate
the electron energies in each layer of IP.

An upward triangular target is irradiated with a laser
pulse (7 J/700 fs) at an intensity 2.3×10^{18} W/cm^2. An in-
tense signal of electrons is observed with IP layers on the
laser axis. The spatial distribution is shown in Fig. 2 (a)
for the hot electrons with energies over 0.7 MeV. These
electrons are generated by $J \times B$ acceleration due to the
UIL pulse irradiation in s-polarization. The observed im-
ages in the first and second layers of CR-39 are shown in
Figs. 2 (b) and (c). A circular pattern of energetic protons
is observed at the target normal direction resulting from
the TNSA (Fig. 2 (c)). The maximum energy of protons is
estimated to be 5.7 MeV at the target normal direction tak-
ing into account the incidence angle to the detector pack
(23°). The zonal patterns of protons are observed around
the circular pattern as indicated by the arrows in Fig. 2 (b).
The patterns are observed only in the first layer of CR-39.
The schematic of the zonal pattern is shown in Fig. 2 (d).
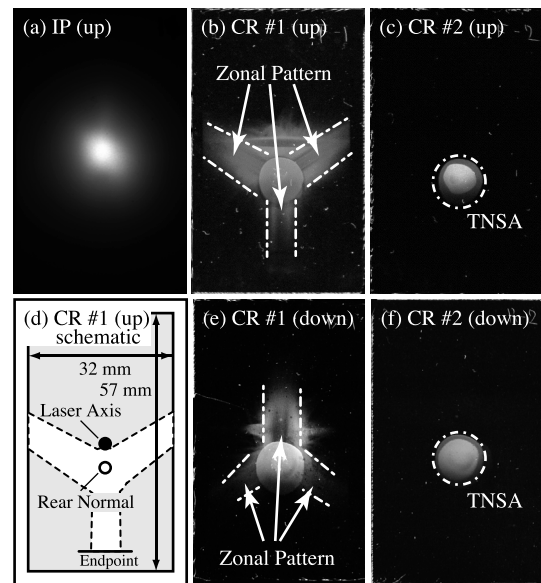The zonal patterns appear to spread out from the target nor-

mal toward the perpendicular direction to each edge of the
upward triangular target.

Next, a downward triangular target is used. The laser
energy and the pulse width are 5 J and 780 fs. The laser
intensity is 1.5×10^{18} W/cm^2. The electron beam is ob-
served again on the laser axis, and the circular protons
are observed at the target normal direction in the second
layer of CR-39 as shown in Fig. 2 (f) even with the target
turned around. These common features for the two differ-
ent settings of targets reveal that the emissions of $J \times B$
accelerated electrons and TNSA protons are insensitive to
the target direction. These features may come from the
long distance from the target edge to the source position
of both electrons and TNSA protons emitting around the
target center. However, the reversed zonal pattern is ob-
served in the first layer of CR-39 for the reversed triangle
as shown in Fig. 2 (e). These results indicate that the proton
beams originate from the target edge.

A 2D PIC code in the XY plane is used to study the
influence of the target edges on the electrostatic field pro-
duction and the proton acceleration. The target consists of
a thin hydrogen plasma with a pre-plasma on the front sur-
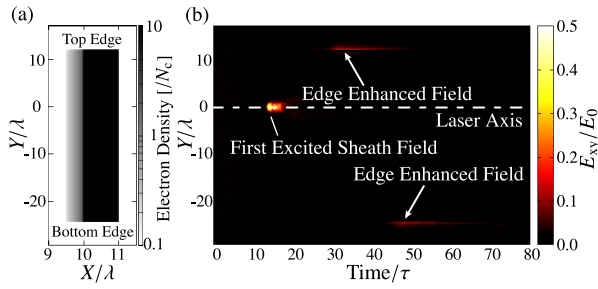face as shown in Fig. 3 (a). The target density and thick-

Fig. 3 (a) Initial plasma density profile. (b) Temporal evaluation of the electrostatic field calculated on the initial surface of the target rear side ($X/\lambda = 11$). The sheath field is produced on the laser axis ($Y/\lambda = 0$) at around 15τ. The strong fields due to the field enhancement are found at the both edges ($Y/\lambda = 12, -24$) as indicated by the arrows after the sheath field spreads on the target rear surface.
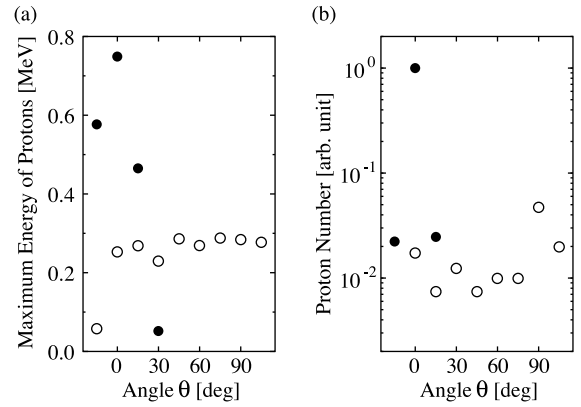

Fig. 4 Simulated emitted direction, $\theta = \arctan(P_y/P_x)$ vs. (a) proton maximum energy and (b) proton number at $t = 80\tau$. Solid circles ($\bullet$) are the target normal sheath accelerated (TNSA) protons. Open circles ($\circ$) are the top edge accelerated protons. $\theta = 0°$ corresponds to the target normal and $\theta = 90°$ corresponds to the $+Y$ direction. The number of protons with energies from 0.15 to 0.30 MeV is counted. TNSA protons are not detected for angle, $|\theta| > 30°$.

ness are set as $10N_c$ and λ, respectively. Here, N_c is the critical density for the 1.053 μm laser wavelength λ. The maximum density of the pre-plasma is $2N_c$. The density decreases exponentially with the 0.2λ scale length in 0.5λ thickness. The target width, i.e. the full length in Y direction, is 36λ. In the simulation, all species (electron and proton) are treated as mobile particles.

The polarization of the laser pulse is parallel to the Z axis. The pulse interacts with plasmas at the normal incidence. The pulse has a Gaussian spatial profile in the transverse direction (Y). The diameter of the focal spot is 2λ in the full width at half maximum (FWHM). The laser pulse irradiates the target at $Y = 0$, and an edge (top edge) is set to be at $Y = 12\lambda$. Another edge (bottom edge) is set at $Y = -24\lambda$. The distance from the laser focusing point to the bottom edge is two times longer than that of the top edge. This scale corresponds to the ratio of the experimental condition. The temporal profile of the laser pulse is a trapezoid shape with 1.2τ rise and fall time. Here, τ is a laser oscillation period. The maximum of a normalized vector potential of the laser pulse ($a = eE_0/(m_0c\omega)$) is 2.0 within the duration 4τ. Here, ω is the laser angular frequency and E_0 indicates the electric field strength of the irradiated laser pulse, 6 MV/μm. e, m_0, and c are the charge of electron, the rest mass of electron, and the speed of light, respectively. The spatial pulse length 4λ is much shorter than the distance from the focusing point to the target edges 12λ or 24λ. We choose the PIC conditions as close as possible to the experiment for allowable calculation capacity.

The temporal evolution of the sheath filed is investigated on the initial surface of target rear side. The strength of the electric field, $E_{xy} = \left(E_x^2 + E_y^2\right)^{1/2}$ is plotted as a function of time and position in the transverse direction as shown in Fig. 3 (b). The sheath field up to 3 MV/μm is produced at the cross point of laser axis and target rear surface at around 15τ because of the charge separation caused by

the hot electrons departure from the target. The directions of the field around the laser axis are normal to the target rear surface. The sheath field spreads out on the target rear surface in time with a velocity $0.8 \sim 0.9c$. The strong fields appear at the target edges later in time indicated by the arrows in Fig. 3 (b). Such strong fields are produced because of the field enhancement caused by the sharp plasma structure at the target edges. The maximum strength of the field at the top edge is 1 MV/μm and is 50% higher than that produced at the bottom edge. This difference is due to the fact that the distance from the electron departing point to the top edge is half the distance from the electron departing to the bottom edge.

Protons are accelerated by the enhanced fields at the target edges. The number and the maximum energy of protons emitted from the target rear surface and the top edge at $t = 80\tau$ are shown as a function of the emission direction in Fig. 4. Here, the angle of emission direction is defined as $\theta = \arctan\left(P_y/P_x\right)$, where P_x (P_y) is the proton momentum in X (Y) direction. Then, $\theta = 0°$ corresponds to the target normal direction and $\theta = 90°$ corresponds to the $+Y$ direction. The protons are identified by their origin as the TNSA protons (solid circle) or the protons accelerated at around the top edge (open circle). Here, most protons emitted at $\theta < 30°$ are accelerated from the target rear surface, namely TNSA protons. The protons accelerated by the target top edge, namely edge protons, are emitted in wide angles from 0° to over 90°. The maximum energies of the top edge protons seem insensitive to the emitted angles in a wide range and are ~ 0.3 MeV as shown in Fig. 4 (a). The maximum proton energy emitted from the top edge is 40% higher than that from the bottom edge. This energy differ-

ence is consistent with the difference of the produced field strength at the target edges descried above. The proton number with the energies up to 0.3 MeV is also insensitive to the emitted angles as shown in Fig. 4 (b). The simulation results clearly reproduce the proton emission in wide angles as observed in the experiments.

In this 2D simulation, the proton emission in the Z direction (parallel to the edges) is negated. When the proton acceleration at the target edges is considered in 3-dimensional (3D) geometries, the sheath field along the Z direction, E_z, may affect the proton emission pattern. However, since the edge length is almost infinite compared to the target thickness, the sheath fields parallel to the edge (E_z) should be negligible compared to the E_{xy} which cause the zonal patterns in the simulation. This is fully consistent with the observed zonal patterns in the experiments.

We evaluate the energy of protons in the observed zonal patterns. From the results of PIC simulations, the maximum energies of the edge protons are almost constant in wide angles. Thus assuming that the protons have a constant maximum energy for the zonal patterns in the experiments, we make use of the endpoint indicated in Fig. 2 (d) for the energy evaluation. The endpoint is defined as follows. The proton emitting in wide angles impinges on the aluminum filter at an oblique angle. At some angle, proton with a given energy may be stopped within the filter and does not reach the CR-39 because of the thickness increase due to the oblique incidence. Here, the endpoint of zonal pattern shown in Fig. 2 (d) exists at 40° from the target normal direction. Then the energy for the zonal patterns is estimated to be 1.4 MeV taking account of the stopping range and the filter thickness in the experiments.

A 2D simulation geometry treats the field spreading on the surface in only up and down directions, namely one dimension. In a real 3D geometry, the field spreading may occur in the two dimensions on the target rear surface, resulting in more reduction of the field production at edges. Then the energy of edge protons in 2D simulations could be higher than the results of 3D simulations and/or the experiments. Actually, the energy ratio becomes 0.25 in the experiments evaluating from the energies of TNSA protons (5.7 MeV) and edge protons (1.4 MeV). The ratio becomes 0.37 in the 2D simulation from Fig. 4 (a), higher than the experiments. This difference may be caused by the dimen-

sional effect. The 3D effect could also emphasize the difference of the field enhancement between the near and far edges. The zonal patterns are found in the perpendicular directions for the closest edges in the experiments. The results imply that the another edge could be too far to lead the effective field enhancement to accelerate protons.

In summary, zonal patterns of protons are observed when triangular targets are irradiated by an UIL pulse with an intensity $\sim 2 \times 10^{18}$ W/cm^2. The proton energy for the zonal pattern is estimated as 1.4 MeV. The generation mechanism of the proton zonal pattern is studied in detail using 2D PIC simulations. The electrostatic field enhancement is found at the target edges. The enhanced fields accelerate protons in wide angles with an almost constant energy and constant number resulting in the zonal patterns, fully consistent with the experiment.

[1] M. Roth *et al.*, Phys. Rev. Lett. **86**, 436 (2001).
[2] M. Temporal, J.J. Honrubia and S. Atzeni, Phys. Plasmas **9**, 3098 (2002).
[3] M. Borghesi *et al.*, Phys. Plasmas **9**, 2214 (2002).
[4] L. Romagnani *et al.*, Phys. Rev. Lett. **95**, 195001 (2005).
[5] A.J. Mackinnon *et al.*, Phys. Rev. Lett. **97**, 045001 (2006).
[6] K. Nemoto *et al.*, Appl. Phys. Lett. **78**, 595 (2001).
[7] S. Fritzler *et al.*, Appl. Phys. Lett. **83**, 3039 (2003).
[8] V. Malka *et al.*, Med. Phys. **31**, 1587 (2004).
[9] W. Luo *et al.*, Med. Phys. **32**, 794 (2005).
[10] S.C. Wilks *et al.*, Phys. Plasmas **8**, 542 (2001).
[11] R.A. Snavely *et al.*, Phys. Rev. Lett. **85**, 2945 (2000).
[12] A. Pukhov, Phys. Rev. Lett. **86**, 3562 (2001).
[13] J. Fuchs *et al.*, Nature Phys. **2**, 48 (2006).
[14] Z.L. Chen *et al.*, Phys. Rev. **E 71**, 036403 (2005).
[15] F.N. Beg *et al.*, Phys. Plasmas **11**, 2806 (2004).
[16] T.E. Cowan *et al.*, Phys. Rev. Lett. **92**, 204801 (2004).
[17] H. Schwoerer *et al.*, Nature **439**, 445 (2006).
[18] M. Zepf *et al.*, Phys. Rev. Lett. **90**, 064801 (2003).
[19] K.A. Tanaka *et al.*, Rev. Sci. Instrum. **76**, 013507 (2005).
[20] http://www.SRIM.org/ , see also J.F. Ziegler, J.P. Biersack and U. Littmark, *The Stopping and Range of Ions in Solids* (Pergamon, New York, 1985).
[21] I. Kawrakow, Med. Phys. **27**, 485 (2000).